Applied Chemical Engineering (2026) Volume 9 Issue 2 ISSN: 2578-2010 (O)
doi: 10.59429/ace.v9i2.5977

RESEARCH ARTICLE

Synergistic Enhancement of Optical and Antibacterial Properties in PMMA-GO-Fe2O3 Nanocomposites: Experimental and Theoretical Insights

Noor Al-Huda S. Hadi*, Hayder M. Abduljalil, Hussein Hakim Abed

Department of Physics, College of Sciences, University of Babylon, Babylon, Iraq

***Corresponding author:** Noor Al-Huda S. Hadi, sci267.noor.saleh@student.uobabylon.edu.iq

ABSTRACT

This work investigates the effect of incorporating graphene oxide (GO) and iron oxide (Fe_2O_3) nanoparticles into poly (methyl methacrylate) (PMMA) on the structural, optical, electronic, and antibacterial properties of PMMA. Experimentally, PMMA/GO/Fe_2O_3 nanocomposite films with different nanofiller concentrations were prepared using the casting method and characterized by Fourier-transform infrared spectroscopy (FTIR), UV–visible spectroscopy, and antibacterial cell-count analysis. Theoretically, density functional theory (DFT) and time-dependent DFT (TD-DFT) calculations were employed to evaluate geometrical structure, HOMO, and LUMO energy levels, density of states (DOS), molecular electrostatic potential (MEP), and optical absorbtions.

The results revealed strong interfacial interactions between PMMA, GO, and Fe_2O_3, confirmed by FTIR peak shifts and Fe–O vibration bands. Optical measurements showed enhanced absorbance, reduced optical band gap, and increased refractive index, dielectric constant, and optical conductivity with increasing nanofiller concentration. DFT and TD-DFT calculations supported the experimental observations by demonstrating reduced HOMO–LUMO gaps, charge redistribution, and enhanced charge-transfer interactions after incorporation of GO and Fe_2O_3. Antibacterial analysis showed significant suppression of bacterial growth, reaching more than 99% inhibition at higher nanofiller loading.

The aim of this work to establish a correlation between the experimentally observed optical and antibacterial behavior and the electronic-structure modifications predicted by density functional theory (DFT) and time-dependent DFT (TD-DFT) calculations, in order to evaluate the potential of PMMA/GO/ Fe_2O_3 nanocomposites for advanced optoelectronic and biomedical applications.

Keywords: GO; PMMA; Nanostructures; DFT; DOS; MEP; Antibacterial Activity.

ARTICLE INFO

Received: 10 April 2026
Accepted: 9 May 2026
Available online: 17 June 2026

1. Introduction

Polymer nanocomposites have recently attracted considerable attention due to their optical and dielectric tenability, potential antibacterial functionality, particularly in biomedical and healthcare-related applications [1]. Bacterial adhesion and subsequent biofilm formation on polymeric surfaces remain major challenges in medical devices, wound dressings, dental materials, and implantable systems, often leading to persistent infections and device failure [2,3]. Consequently, imparting intrinsic antibacterial activity to widely used polymers such as (PMMA) has become an important research objective.

PPMMA is one of the most extensively utilized synthetic polymers owing to its semi amorphous structure, exceptional optical transparency, low density, ease of processing, and high chemical and thermal stability [4,5]. These advantages have enabled its widespread application in optical, medical, electrical, and optoelectronic fields [4, 6–9]. Furthermore, PMMA exhibits low dielectric permittivity and loss, high surface hardness, good weather resistance, excellent environmental inertness, and outstanding biocompatibility, making it suitable for diverse industrial and biomedical uses [10,11]. Despite these favorable properties, PMMA inherently lacks antibacterial activity, which promotes microbial colonization on its surface, particularly in moist biological environments [11–13]. To overcome this limitation, the incorporation of functional nanofillers with antimicrobial activity has emerged as an effective and sustainable strategy [14]. Among various candidates, (GO) and (Fe_2O_3) nanoparticles have demonstrated strong antibacterial potential duo to their unique physicochemical characteristics. GO is particularly attractive for polymer modification because of its large specific area, high electrical conductivity, and surface rich in oxygen-containing functional groups [15,16]. These features allow GO to significantly enhance the mechanical, thermal, electrical, and optical properties of polymer matrices, in addition to contributing to antibacterial performance [17–19].

Similarly, Fe_2O_3 nanoparticles are considered promising nanomaterials owing to their distinct optical and magnetic properties, biocompatibility, and suitability for applications in biomedicine, water purification, magnetic storage, and sensing technologies [20–22]. The incorporation of Fe_2O_3 into polymer matrices has also been reported to influence light absorption behavior and energy band gap characteristics, depending on the nanoparticle concentration and dispersion [23]. By integrating both GO and Fe_2O_3 into a PMMA matrix, hybrid nanocomposites with synergistically enhanced optical, electrical, and antibacterial properties can be achieved, outperforming the individual components [24–26].

In medical and dental applications, where surface-associated bacterial colonization can cause illness and implant failure, the development of polymer-based biomaterials with inherent antibacterial qualities has drawn more attention [27], because to its simplicity of manufacture, mechanical stability, and biocompatibility, (PMMA) continues to be one of the most popular polymers in these disciplines [7]. However, because of its intrinsic lack of antibacterial action, functional nanomaterials that can stop microbial growth must be added, because of their distinct physicochemical characteristics and proven antibacterial capabilities, nanoparticles like Fe2O3 and GO have become intriguing additions [28, 29].

Quantitative evaluation of antibacterial behavior is commonly achieved using colony-forming unit (CFU) cell-count analysis, which provides a direct and reliable measurement of viable bacterial cells after exposure to the tested material [30–32]. This method enables precise assessment of nanoparticle concentration–dependent antibacterial efficiency and allows correlation between material composition and biological response [33]. Consequently, investigating the antibacterial performance of PMMA reinforced with Fe_2O_3 and GO using CFU-based analysis is essential for establishing its suitability for biomedical applications requiring infection-resistant surfaces, by measuring decreases in bacterial viability in contrast to a control, this technique allows precise comparisons of antibacterial efficiency across various nanofiller doses [34, 35]. A number of methods of microbial suppression, such as the production of reactive oxygen species (ROS) from Fe_2O_3 nanoparticles, membrane disruption from GO sheets, or synergistic effects from their combined dispersion within the PMMA matrix, might be reflected in variations in CFU counts.

Molecular electrostatic potential (MEP) is a key descriptor of chemical reactivity, charge transfer behavior, and intermolecular interactions. It also offers a direct picture of the distribution of charges over a molecular surface [36, 37]. MEP is especially useful for evaluating surface polarity and electrostatic activity in complex nanostructures because in contrast to total charge analysis, it represents the combined effects of nuclear charges and electron density [38].

With an emphasis on the process of the ensuing changes and their relationship to the material's nanostructure, using DFT and TD-DFT, the study's theoretical portion clarifies the electronic, optical, and electrostatic processes of nanocomposites. It examines PMMA, GO, and GO-FeO-PMMA’s geometrical structure, HOMO and LUMO orbitals, energy band gaps, DOS, UV-Vis. spectra, and MPE. The results show that adding Fe_2O_3 and GO improves optical absorption, dielectric response, and antibacterial activity via changing electronic structure, enhancing charge transfer, and narrowing band gaps. Furthermore, the theoretical findings provide insight into the multi-functionality fueled by electronic structures in these nanocomposites by correlating with experimental optical measurements and antibacterial activity.

This work theoretically and experimentally examines the impact of adding Fe_2O_3 and GO to the PMMA matrix on the structural, electronic, and optical characteristics. Comprehending these impacts is essential to creating customized high-performance nanomaterials tailored for future applications.

Although several previous studies have separately examined PMMA/GO or PMMA/metal oxide systems, limited attention has been given to the simultaneous integration of GO and Fe_2O_3 within a PMMA matrix together with a direct correlation between experimental observations and DFT/TD-DFT electronic-structure analysis. Therefore, the novelty of the present work lies in the combined investigation of optical and antibacterial performance supported by theoretical calculations including HOMO and LUMO levels, DOS, MEP, and optical absorbtion. This integrated approach provides deeper understanding of how interfacial electronic interactions and charge-transfer mechanisms govern the multifunctional behavior of PMMA/GO/Fe_2O_3 nanocomposites, highlighting their potential for advanced optoelectronic and biomedical applications.

2. Materials and methods

2.1. Materials

PMMA was used in granular form and was procured with high purity (99.99%) from (800000 M.W.), GO was predicated by group that described in details in the previous publications ,where the size of GO was between 94.49 nm to ~2µm of the surface area and 0.700 nm of the thickness, Fe_2O_3 nanoparticles used as powder from US Research Nanomaterials, and chloroform were used as the primary materials for the preparation of nanocomposites. All chemicals were of analytical grade and used without further purification.

2.2. Preparation of PMMA-GO-Fe2O3 Nanocomposites

PMMA solution was prepared by dissolving 1 g of PMMA in 30 mL of chloroform under continuous stirring for 15 minutes at room temperature until a homogeneous solution was obtained. For nanocomposite preparation, GO and Fe_2O_3 nanoparticles were incorporated into the PMMA solution at different weight percentages (1wt%, 2wt%, 3wt%, and 4wt%). The resulting mixtures were continuously stirred for 15 minutes to ensure uniform dispersion of nanoparticles. The prepared solutions were cast into glass Petri dishes (10 cm diameter) and left to dry under ambient conditions to form uniform nanocomposite thin films.

2.3. Methodology

Theoretically, three nanostructures PMMA, GO, and GO-FeO-PMMA are generated using a nanotube modular program and visualized with Gaussian View 5.0 as shown in Figure1, where illustrates the optimized geometrical structures of the investigated nanostructures obtained from density functional theory (DFT) calculations, including GO, GO–FeO, and GO–FeO–PMMA systems. The figure demonstrates the structural evolution after incorporation of iron oxide and PMMA into the GO framework and highlights the interfacial interactions among the constituent components. The optimized GO structure exhibits oxygen-containing functional groups such as hydroxyl, epoxy, and carboxyl groups distributed over the graphene surface, which provide active sites for interaction with FeO clusters and PMMA chains. After incorporation of FeO, noticeable structural rearrangement and charge redistribution occur around the Fe–O bonding region, indicating strong interaction between iron oxide and oxygenated GO functional groups. DFT and TD-DFT are used to model their structural, optical, and electronic characteristics using the Gaussian 09 software [39]. GaussSum 2.2 software is used to extract the DOS, and OriginLab 2024b. is used for generating graphs of the electronic characteristics. Calculations were performed under optimized conditions, applying the 6-31G-B3LYP functional to determine key electronic properties such as HOMO and LUMO levels, LUMO-HOMO gap (Eg), bond lengths, and bond angles [40].

2.4. Antibacterial Activity

The material's antibacterial effectiveness against staphylococcus aureus biofilm formation on burn and wound specimens was assessed after 24 hours. Five sets of 10 sterile specimens were used for this purpose. In order to activate the bacterial pellet, it was submerged in two milliliters of nutritional broth and incubated in an aerobic, sterile tube at 37°C for two hours. After that, 100 µL of the bacterial suspension was added to 10 mL of nutritional broth, and the mixture was cultured for 24 hours. After that, the sample and 9 mL of nutritional broth were combined with 1 mL of bacterial solution, and the mixture was incubated for 24 hours. Using a spectrophotometer (Lambda 25, UV/VIS Spectrophotometer, PerkinElmer, Shelton CT, USA) to measure the absorbance (abs.) value at a wavelength of 600 nm, the extracted bacteria's turbidity was determined to be 0.5 McFarland (1.5 × 108 colony-forming units per milliliter (CFU/mL)). To get rid of non-adherent cells, each sterilized disc specimen was then removed from the bacterial mixture and washed twice with PBS (pH=7.2). The material was then put in a tube with 10 mL of sterile saline solution, and the adherent bacterial cells were dispersed for 10 minutes using a vortex. The dilution solution was then pipetted out (0.1 mL) over the nutrient agar plate's surface following a serial dilution up to (10^{-3}). The dilution solution (0.1 mL) was then pipetted over the nutrient agar plate's surface. The plates were then incubated in anaerobic conditions for 24 hours at body temperature (37°C). To verify the consistency of the experimental groups' anti-biofilm effect, the test was conducted three times. The number of CFU/mL of growing bacteria was ascertained using a direct cell culture method as in previous studies [41, 42].

2.5. Theoretical part

This research includes essential equations used to analyze the optical properties of polymers, particularly focusing on energy gap, absorbance, reflectance, transmittance, absorption coefficient, and refractive index, real and imaginary dielectric constant. These parameters are critical for understanding the optical behavior of polymeric materials.

The absorption coefficient (α) is calculated by using the relation [43]:

$$\alpha = \frac{2.303\,A}{t} \tag{1}$$

Where t is the thickness of the sample, and A the absorbance. The energy gap for a non-direct transition is determined by using Tauc's equation [44]

$$\alpha h\nu = B(h\nu - E_g)^m \tag{2}$$

Where B is a constant, hν is the photon energy, Eg is the energy gap, and (m = 2, 3) for allowed and forbidden indirect transition, respectively (which is appropriate with polymer nanocomposites prepared by the casting method).

The extinction coefficient (K) is determined by the relation [45]:

$$K = \frac{\alpha\lambda}{4\pi} \tag{3}$$

Where λ is the wavelength

The refractive index (n) is calculated by the formula [46]:

$$n = \left(\frac{4R}{(R-1)^2} - K^2\right)^{1/2} - \frac{R+1}{R-1} \tag{4}$$

Where R is the reflectance.

The real (ε_1) and imaginary (ε_2) parts of the dielectric constant are calculated by the relations [47]:

$$\varepsilon_1 = 2nK \tag{5}$$

$$\varepsilon_2 = n^2 - K^2 \tag{6}$$

Nanostructures	**Relaxation structures**
PMMA	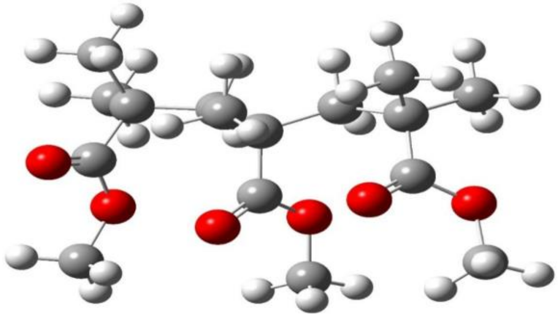
GO	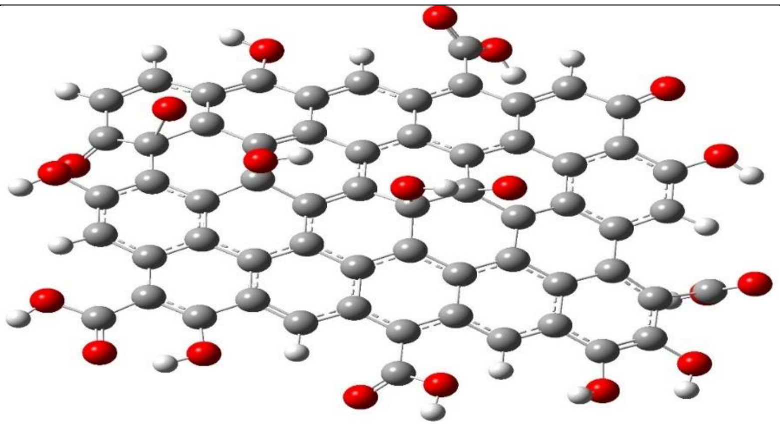
GO-FeO	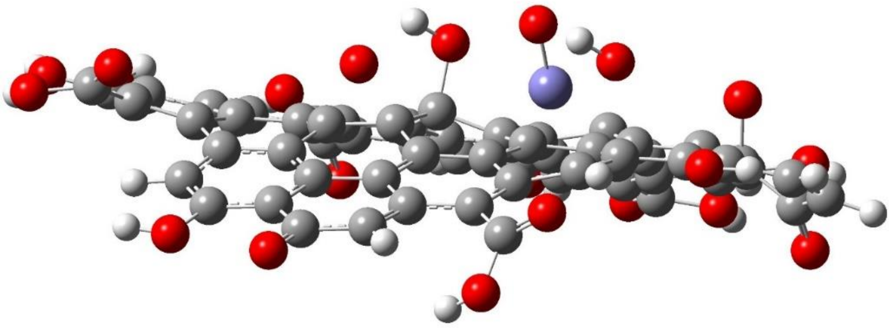
GO-FeO-PMMA	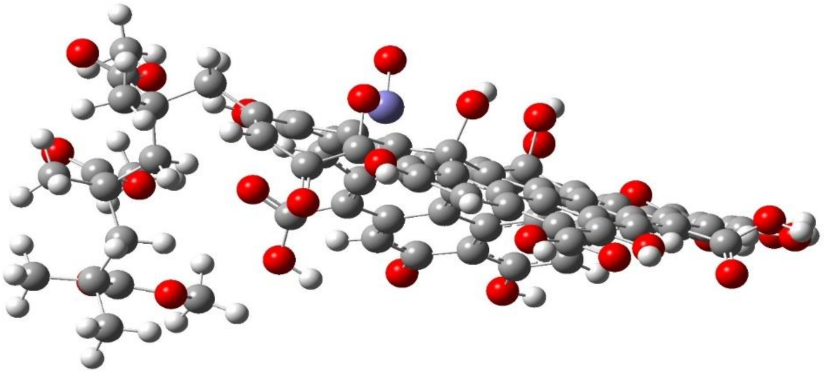

Figure 1. The geometrical structures for the nanostructures.

3. Results and Discussions

3.1. Theoretical part

3.1.1. Geometrical structures

The geometrical characteristics of the PMMA, GO, and GO-FeO-PMMA nanostructures will be examined in this section. Table 1 displays the geometrical properties of the atoms' bond lengths and bond angles. The atoms in PMMA nanostructures from C-H, C-C, C-O, and C=O, also, GO form C-C, C=C, C…C, C-O, C=O, H-O, and C-H bonds, according to the DFT calculations. Additionally, the GO-FeO-PMMA had unevenly shaped surfaces. The atoms inside the nanostructures showed a variety of unique interatomic angles, according to angle measurements.

The results indicate that incorporation of FeO and PMMA into the GO framework produces noticeable variations in bond lengths and bond angles compared with pristine GO.

Table 1. listed the bond lengths and angles between atoms for the nanostructures.

Nanostructures	Bond type	Bond lengths (Å)	Angle type	angles (°)
PMMA	C-H	1.08	C-C-H	114.2-117
	C-C	1.42-1.5	C-C-C	113.8-119.7
	C-O	1.43	O=C-C	119.1-120.8
	C=O	1.22	O=C-O	121.8-122.1
			H-C-H	106.7-108.8
GO			C-C-C	114.3-119.4
			C-C…C	115.5-122.2
		1.42-1.51	C…C…C	118.1-121.5
	C-C	1.3	C-C-O	61-118.9
	C=C	1.38-1.40	C=C-C	119.5-123.7
	C…C	1.43	C-C…C	120.5-123.6
	C=O	1.22	O=C-O	117.0-121.5
	C-H	1.08	O=C-C	121.5-126.1
	H-O	`1.0-0.97	C-O-H	106.2-113.6
			C…C-H	116.7-121.1
			C=C-H	117.9-122.0
			C-C-H	114.2-117.0
GO-FeO			C-C-C	107.6-120.2
			C=C=C	118.2-122.3
			C-C=C	117.4-125.4
	C-C	1.42-1.5	C-C…C	112.9-124.5
	C=C	1.38-1.4	C…C…C	113.4-124.1
	C···C	1.40	C=C-H	119
	C-O	1.43	C…C-H	117.6-118.5
	C=O	1.24	C-O-H	108.7-110.2
	C-H	1.07	C-C=O	118.6-120.7
	Fe-O	1.82	C=C=O	120.5
	H-O	0.96	C…C=O	120.2
	Fe-C	1.92	C…C-O	108.1-120.0
			C=C-O	118.9-120.5
			C-C-O	102.9-111.4

			C-Fe-O	179.9
			C-C-Fe	109.5
GO-FeO-PMMA			C-C-C	108-120.4
			C=C=C	118.7-121.9
			C-C=C	117.1-125.8
			C-C…C	113.1-124.2
	C-C	1.45-1.58	C…C…C	113.9-123.7
	C=C	1.33-1.37	C=C-H	118.5-119.9
	C…C	1.38-1.44	C…C-H	118
	C-O	1.41-1.44	C-O-H	108.7-109.8
	C=O	1.26	C-C=O	118.7-121
	C-H	1.05	C=C=O	120.7
	H-O	1.92	C…C=O	120.24
	Fe-O	1.8	C…C-O	102-120.5
	Fe-C	0.95	C=C-O	119.2-120.5
			C-C-O	102.9-111.4
			C-Fe-O	180.2
			C-C-Fe	109.7
			C…C-Fe	107.3

3.1.2. HOMO and LUMO levels, and energy gap

In this section, the HOMO and LUMO energy levels, along with the energy gap, are analyzed as key parameters for understanding electron transport between energy bands. The energy gap also provides insight into the electronic nature of the nanostructures or molecules. The HOMO and LUMO levels, as well as the energy gap of the studied nanostructures were calculated using DFT underground-state conditions. The obtained values are summarized in Table 2.

Table 2. Indexed the HOMO and LUMO energy levels, and energy gap of the nanostructures.

Nanostructures	HOMO (eV)	LUMO (eV)	Energy Gap (eV)
PMMA	-7.08	-0.16	6.92
GO	-5.58	-4.11	1.47
GO-FeO	-5.613	-4.456	1.157
GO-FeO-PMMA	-5.7	-4.44	1.26

The electronic distribution was analyzed through the frontier molecular orbitals (HOMO) and (LUMO) for PMMA, GO, GO-FeO, and GO-FeO-PMMA to determine the effect of nanoparticle and polymer modification on the electronic properties of GO. As shown in Figure 2, GO is observed that the distribution of HOMO and LUMO is concentrated around the functional oxygen groups, indicating electronic activity in those areas, which enhances the properties of GO as a semiconductor material. In GO-FeO-PMMA, modification with PMMA changes the distribution of electronic density, as HOMO and LUMO are centered in different areas, indicating spatial separation between energy levels, which may improve the efficiency of charge separation between positive and negative charges and benefit applications in solar cell and photonic materials [40,41]. It is noted that the addition of FeO to GO resulted in a significant decrease in the energy gap (from 1.47 to 1.15 eV), indicating an improvement in electronic conductivity, this result agreement with reference [42].

When PMMA is added to GO–FeO, the gap increases slightly to 1.26 eV, indicating a relativity higher electronic stability. The energy band gap values obtained from the experimental optical measurements and theoretical DFT calculation show the same overall trend, despite differences in their absolute magnitudes. Experimentally, the optical band gap (Eg) determined from Tauc plots decreases systematically from ~4.08 fore pure PMMA to ~3.78 eV for 4 wt% Fe_2O_3-GO-PMMA, indicating progressive band gap narrowing with increasing nanofiller content. This reduction is attributed to the formation of localized defect states, interfacial charge-transfer complexes, and enhanced electronic delocalization induced by Fe_2O_3 and GO within the PMMA matrix. In contrast, the theoretical band gaps, calculated from HOMO–LUMO energy differences using DFT, are significantly lower, with values of 1.47 eV for GO, and 1.26 eV for GO–FeO–PMMA. These lower values arise because DFT evaluates the intrinsic electronic structure at the molecular level, focusing on frontier orbitals under idealized conditions and neglecting excitonic effects, disorder, and phonon interactions that are inherently present in experimental thin films.

Despite this quantitative discrepancy, a strong qualitative agreement exists between experiment and theory. Both approaches confirm that the incorporation of FeO into GO leads to a pronounced reduction in the energy gap due to Fe-O-C hybridization. The slight increase in the theoretical band gap upon PMMA incorporation (from 1.15 to 1.26 eV) reflects enhanced structural stability and partial localization of electronic state, which is consistent with the experimental observation that PMMA moderates- but does not eliminate- the band-gap narrowing effect induced by Fe_2O_3/GO. While the theoretical HOMO-LUMO gap reflects a basic molecular electronic gap, the experimental optical band gap is, all things considered, an effective bulk optical gap. The agreement in trend validates the experimental results and confirms that the observed band-gap narrowing is fundamentally driven by electronic structure modification, interfacial charge transfer, and defect-state formation introduced by Fe_2O_3 and GO. This consistency strongly supports the electronic-structure-driven interpretation of the enhanced optical, electronic, and antibacterial performance of the PMMA/ Fe_2O_3/GO nanocomposites.

From the Figure 2, the majority of the charge density is widely distributed, particularly within GO nanostructure. The calculations demonstrate that electron charge localization primarily occurs around the iron atom. Where incorporating the polymer does not significantly alter the nanostructure, as the charge distribution remains concentrated on the iron atom, DFT results show that the highest localized charge density at the defect site appears in PMMA-GO–FeO nanostructure.

Nano-structures	**HOMO**	**LUMO**
PMMA	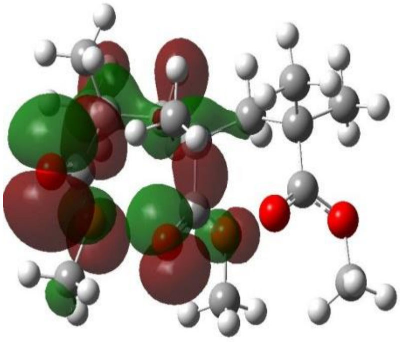	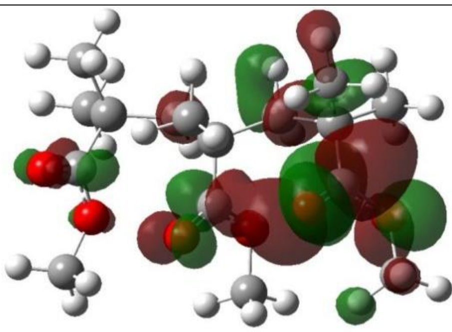

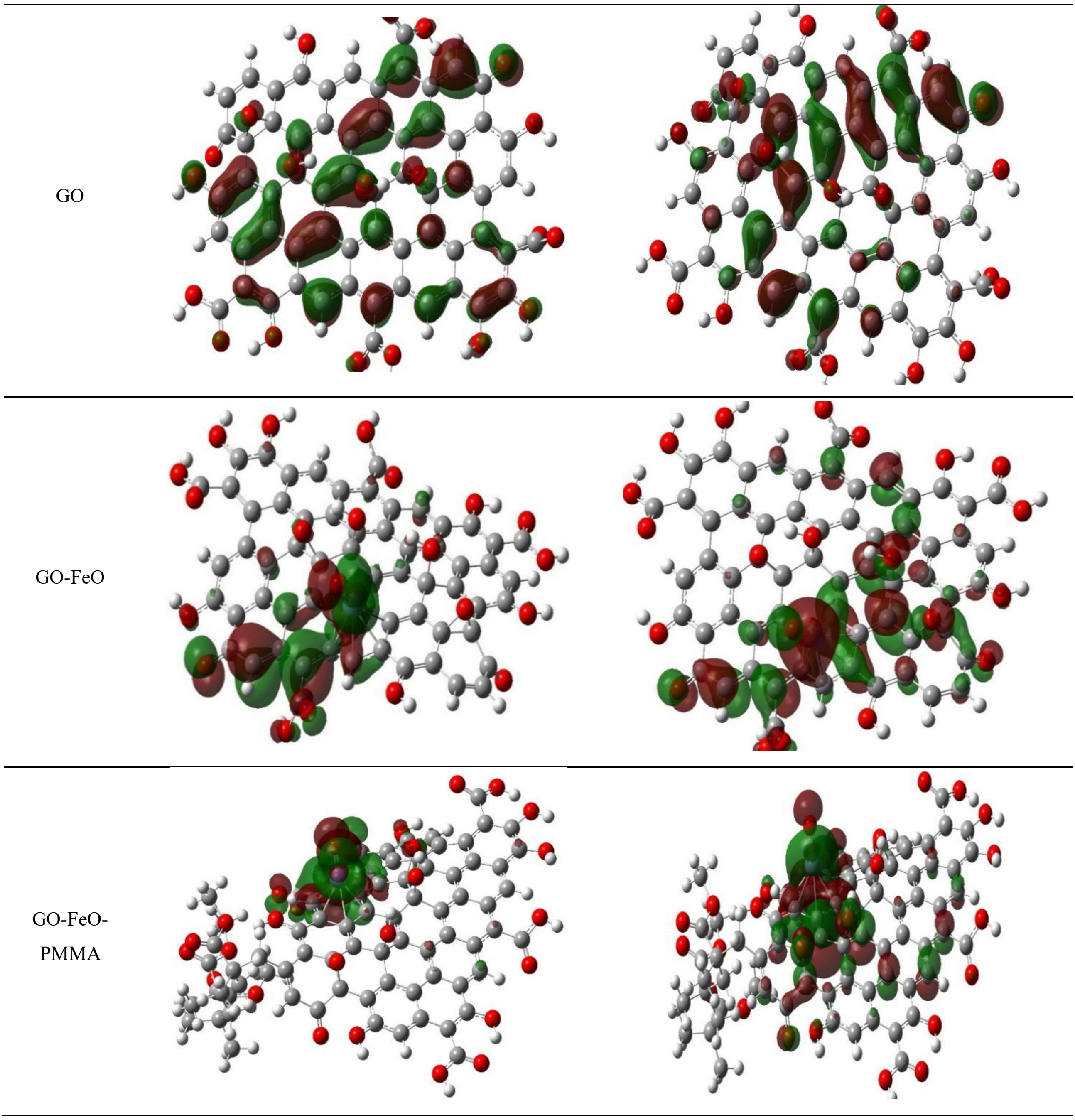

Figure 2. Visualize the charge density distributions for nanostructures.

Figure 3 illustrates the DOS spectra for the GO, and GO–FeO–PMMA nanostructures, obtained using GaussSum 2.2 software. The DOS spectra enable the examination of shifts in molecular orbital energy levels. As shown in Table 2, the HOMO level shifts to higher energy upon the incorporation iron oxide and PMMA. The pristine GO nanostructure, acting as a semiconductor, exhibits a wide energy gap of 1.47 eV in this state.

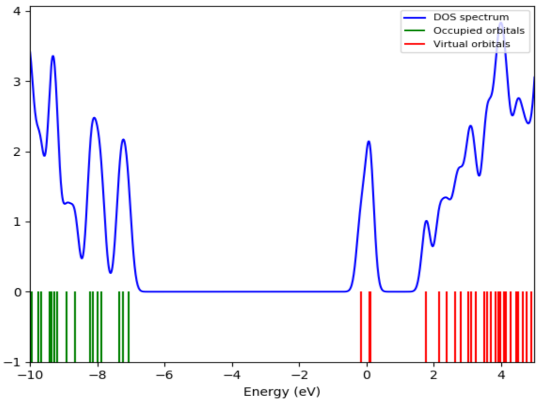

PMMA

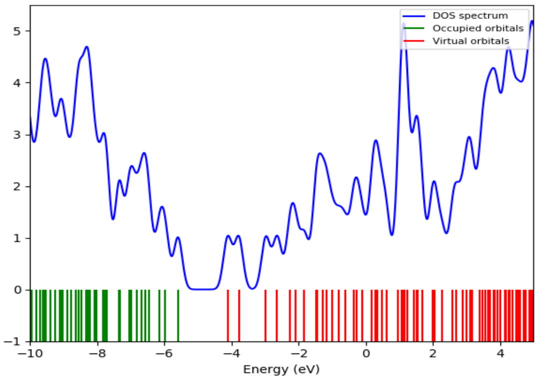

GO

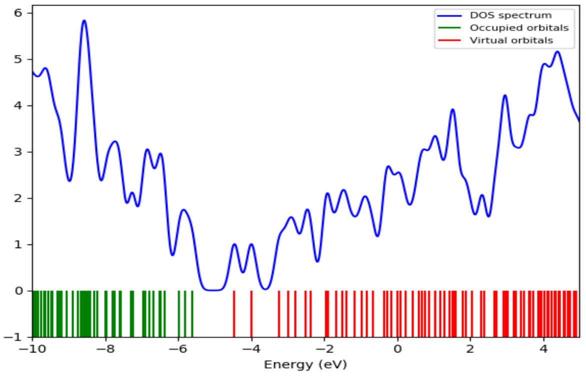

GO-FeO

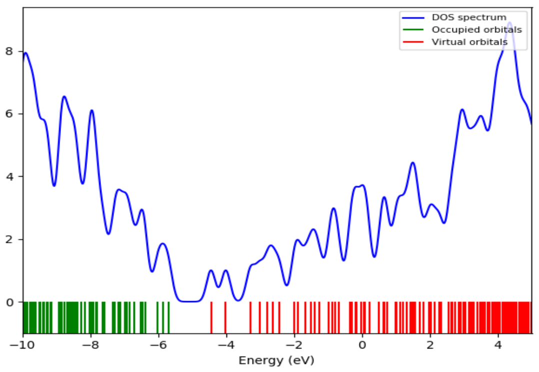

GO-FeO-PMMA

Figure 3. DOS spectrum for the nanostructures.

3.1.3 UV–Visible spectra

In this work, the evaluation of UV-Vis. spectra plays a vital role in assessing the light-harvesting efficiency of the nanostructures and their ability to absorb solar radiation. The UV-visible spectra and oscillator strengths of the excited nanostructures were calculated using the TD-DFT method. To clarify the influence of FeO and PMMA, the UV-Vis. spectra of the investigated nanostructures are presented in Figure 4. The incorporation of FeO and PMMA into GO resulted in a noticeable redshift of the main absorption peak. This behavior arises charge transfer interactions between the GO sheets and FeO domains.

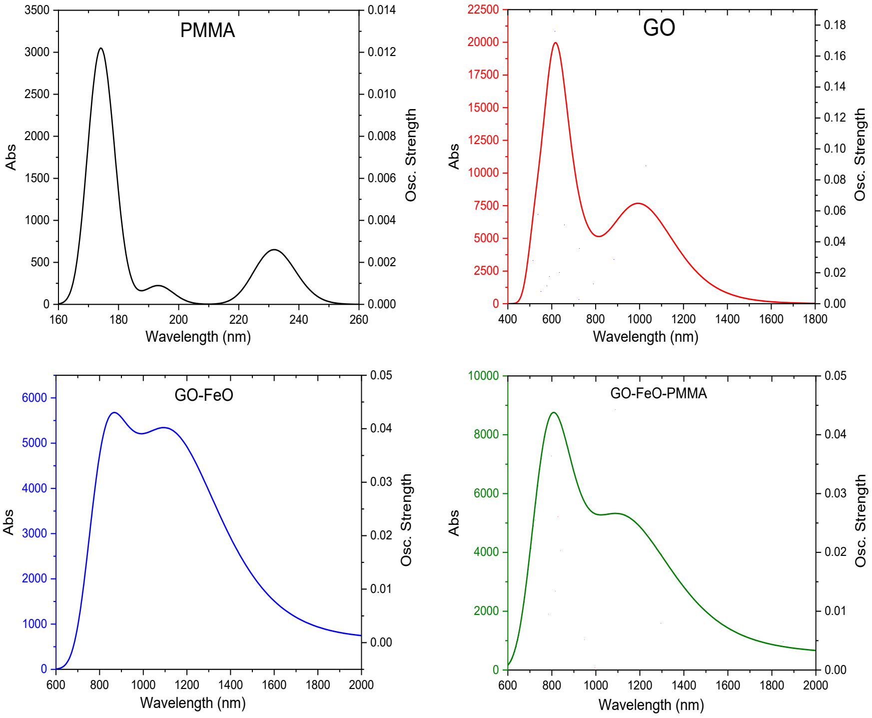

Figure 4. UV–Visible spectra and oscillator strength for nanostructures computed by the TD-DFT method.

The experimental UV–visible spectra and theoretical TD-DFT calculations exhibit strong conceptual agreement, confirming that the optical response of the PMMA/Fe_2O_3/GO nanocomposites is governed by electronic structure modification rather than simple filler absorption. Experimentally, pure PMMA shows week UV absorption and high transparency due to its wide band gap. The interaction of Fe_2O_3 and GO leads to a pronounced increase in absorbance and systematic redshift of the absorption edge, indicating the formation of new electronic states and enhanced charge-transfer interactions within the polymer matrix.

TD-DFT calculations reveal that this behavior originates from π–π^* transitions in GO and Fe-O-C charge transfer excitations introduced by FeO incorporation. The slight modulation observed upon PMMA inclusion arises its insulating nature, which stabilizes the electronic structure without suppressing interfacial charge transfer.

While theoretical spectra consist of discrete excitation peaks and experimental spectra display broadened absorption bands, this difference is attributed to film-level effects such as disorder, phonon coupling, excitonic interactions, and nanoparticle dispersion that are not captured in molecular-scale simulations. Nevertheless, both approaches consistently demonstrate that Fe_2O_3/GO incorporation extends light absorption into the visible region by reducing excitation energy and increasing electronic delocalization. This close agreement validates the electronic-structure-driven origin of the enhanced UV-visible response and supports the tunability of the nanocomposites for optoelectronic and bioactive applications.

3.1.4. Molecular Electrostatic Potential (MEP)

The MEP is an effective descriptor for assessing surface polarity, interfacial charge transfer, and interaction processes in hybrid nanocomposites since it is controlled by the combined effect of nuclear charge and electron density distribution as seen in Figure 5, where PMMA’s MEP shows a very small potential charge, suggesting a weakly polarized electrostatic surface. The carbonyl oxygen atoms (C=O) of the ester groups, where electron density is concentrated because of strong electronegativity, are the primary location for negative potential areas. On the other hand, the methyl groups and polymer backbone exhibit positive potential, indicating areas lacking electrons. The electrostatic potential of PMMA is spatially smooth and continuous, indicating its dielectric nature. This restricted charge separation shows that PMMA alone has minimal inherent electrostatic reactivity, operating largely as an electrostatic stabilizer rather than an active charge giver or acceptor.

GO offers a considerably distinct MEP profile characterized by high electrostatic heterogeneity. Epoxy, hydroxyl, and carboxyl functional groups that include oxygen provide noticeable negative potential areas throughout the GO surface. The carbon lattice and the hydrogen atoms next to oxygen functions are both covered in positive potential areas. This heterogeneous charge distribution represents partial breakdown of the π-conjugated system, resulting to localized electron accumulation and depletion zones. As a result, GO has a larger electrostatic interaction capacity and a higher surface polarity than PMMA, which allows for improved adsorption and interfacial interactions.

The GO–FeO–PMMA system exhibits the greatest stability and electrostatic complexity. PMMA adds a dielectric medium that modifies and redistributes the electrostatic field while the strong positive and negative potential areas created by GO–FeO continue to be predominant. A more homogeneous but increased MEP distribution results from the ester groups of PMMA interacting with charged GO–FeO sites via dipole–charge coupling. Sustained electrostatic activity is encouraged and excessive charge localization is prevented by this equilibrium between charge enhancement and stability. The composite therefore displays better surface polarity, interfacial compatibility, and electrostatic endurance compared to individual elements. The MEP contrast is greatly increased when FeO is added to GO. Whereas prominent positive potential areas are concentrated close to Fe centers, strong negative potential regions are seen surrounding oxygen atoms linked to iron. This results from the metal-oxygen charge transfer process, in which iron atoms, depending on the coordination environment, behave as electron donors or acceptors. Localized electric fields are produced at the GO–FeO contact by interfacial electrostatic dipoles, as seen by the ensuing MEP map. These dipoles demonstrate that FeO functions as an electrostatic activation center inside the composite structure by improving surface reactivity and charge separation.

Nanostructures	**Relaxation structures**
PMMA	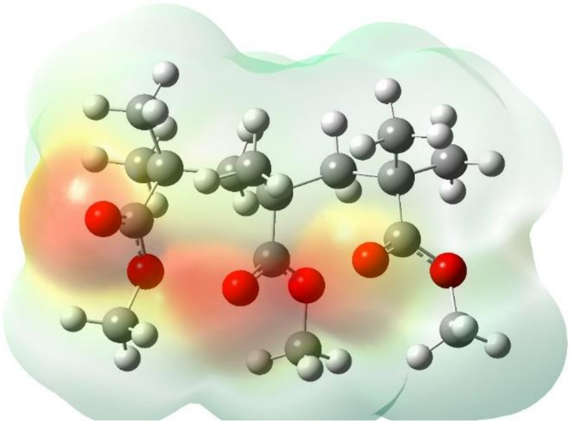

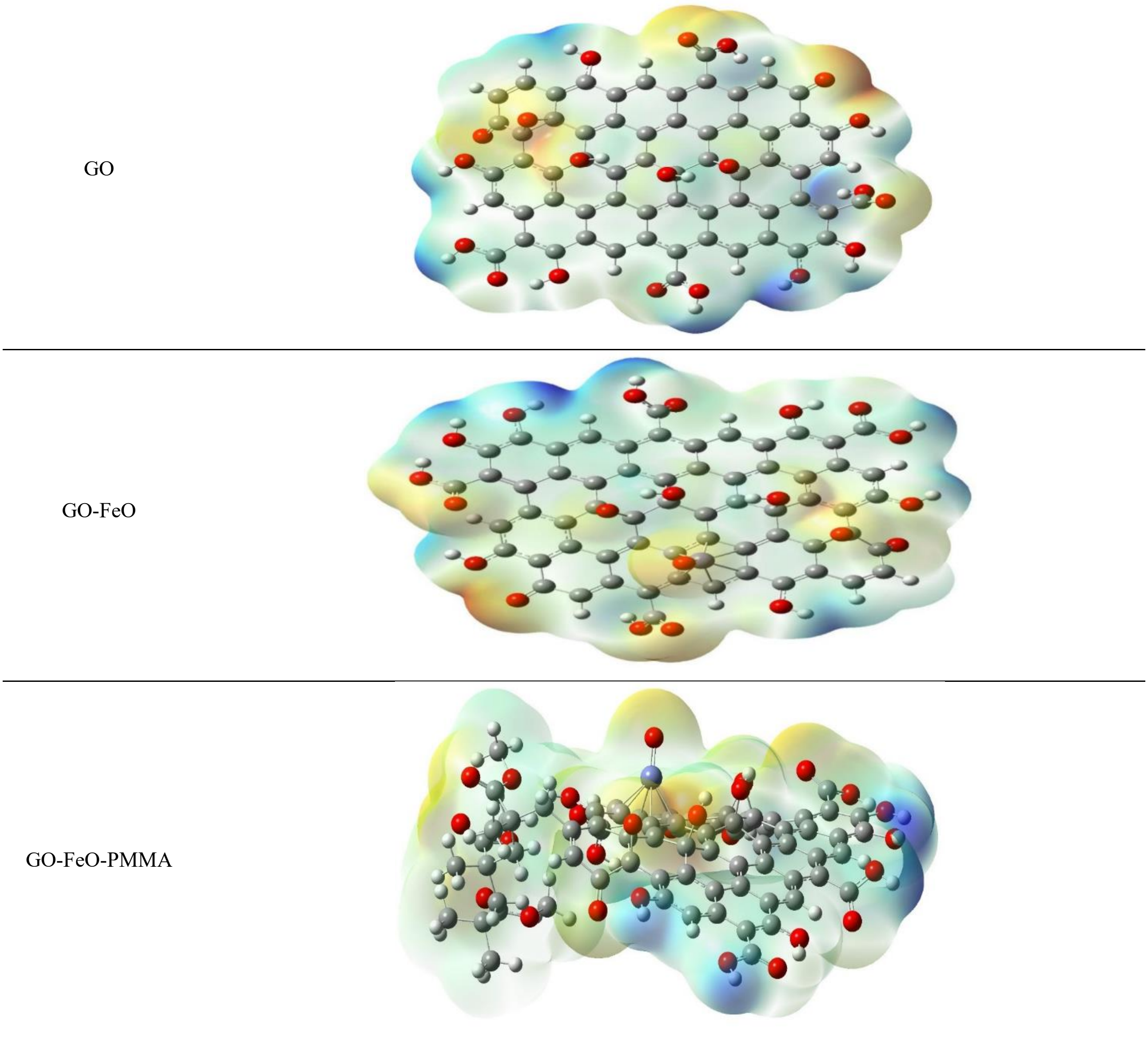

Figure 5. Visualize the Molecular Electrostatic Potential distributions for nanostructures.

The pattern may be seen in the methodical development of electrostatic behavior in the materials under study: (GO<GO–FeO–PMMA<PMMA). The intensity of the electrostatic contact, surface polarity, and charge separation all increase with this process. Through cooperative interactions between GO, FeO, and PMMA, the hybridization technique successfully converts a weakly polar polymer into a highly electrostatically active nanocomposite as in the table 3.

Table 3. Indexed the Molecular Electrostatic Potential of the nanostructures.

Nanostructures	From * e^{-2}	To * e^{-2}
PMMA	-7.107	7.107
GO	-9.176	9.176
GO-FeO	-9.600	9.600
GO-FeO-PMMA	-9.657	9.657

The results regarding HOMO–LUMO, Eg, DOS, UV–Vis, and MEP indicate strong electronic interactions and charge transfer in PMMA/GO/FeO nanostructures. The inclusion of FeO and PMMA in GO leads to orbital delocalization and a reduced HOMO–LUMO gap, which enhances electronic polarizability and charge mobility. The DOS spectra highlight additional states near the Fermi level due to hybridization of GO π-orbitals, Fe d-orbitals, and PMMA states, facilitating electronic transitions. The UV-Vis spectra show increased absorption and redshift due to lowered excitation energy and enhanced charge transfer. MEP maps reveal significant charge redistribution around oxygen and Fe sites, confirming active electronic regions in the hybrid structure.

3.2. Experimental part

3.2.1. Structural properties

The FTIR spectra elucidate the structural changes in PMMA after the addition of Fe_2O_3 and GO. As shown in Figure 6, the pristine PMMA, the strong peaks at 2950–2850 cm^{-1} correspond to the symmetric and asymmetric C–H stretching of CH_2 and CH_3 groups, while the intense absorption at around 1730 cm^{-1} is attributed to the C=O stretching vibration of the ester group, hence affirming the integrity of the PMMA backbone. The peaks at around 1450 cm^{-1} and 1140–1240 cm^{-1} correspond to C–H bending and C–O–C stretching, respectively, both indicative of PMMA's amorphous structure. A number of significant modifications occur upon the introduction of Fe_2O_3/GO nanoparticles: The existence of O–H stretching, which is caused by the hydroxyl and carboxyl groups of GO and surface-bound water on Fe_2O_3, is confirmed by a wide absorption at about 3400 cm^{-1}. PMMA and the oxygenated surface groups of GO and Fe_2O_3 exhibit hydrogen bonding and interfacial dipole–dipole interactions, as evidenced by a discernible shift of the C=O peak from 1730 to around 1720 cm^{-1}. Fe–O stretching vibrations produce a new low-frequency region at around 560–580 cm^{-1}, confirming that Fe_2O_3 nanoparticles were successfully incorporated. Stronger chemical interaction between PMMA and nanofillers is seen by the Fe–O peak intensity strengthening and the C=O band weakening when the Fe_2O_3/GO ratio rises. For enhanced optical and dielectric qualities, this structural hybridization strengthens interfacial bonding and electron delocalization.

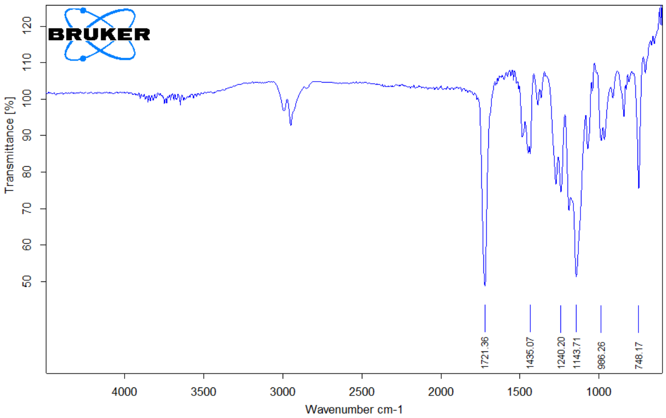

Pure

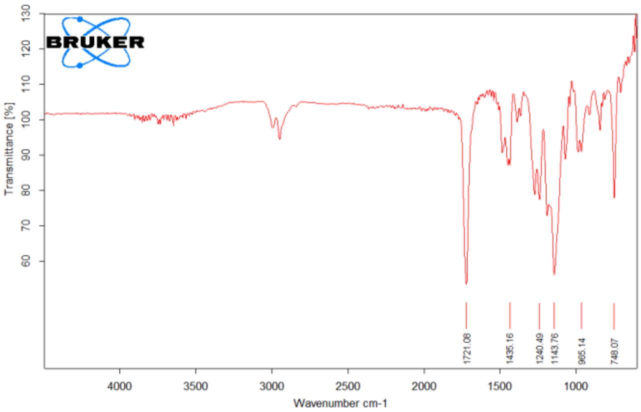

1wt%

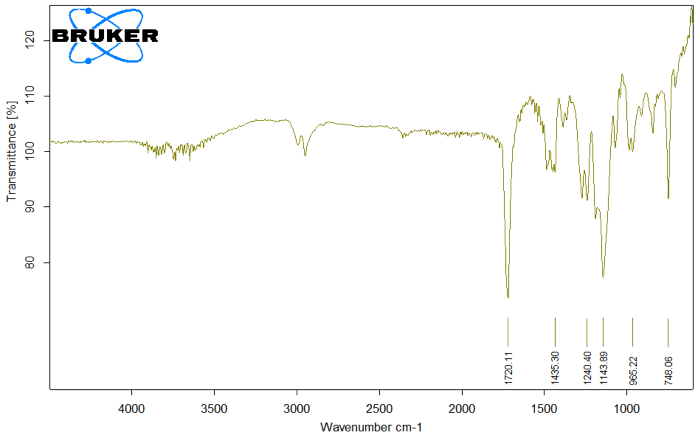

2wt%

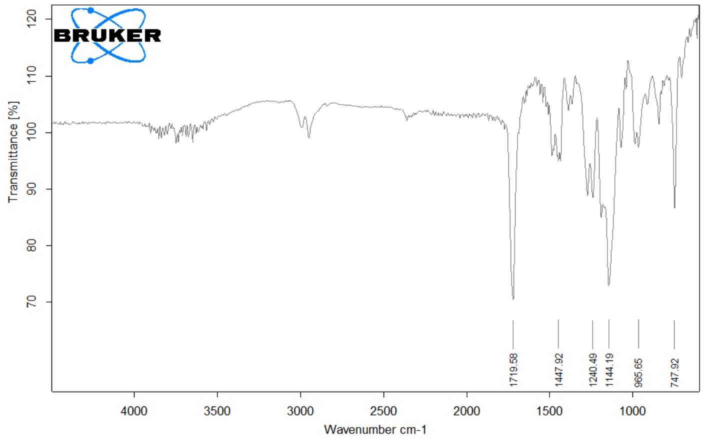

3wt%

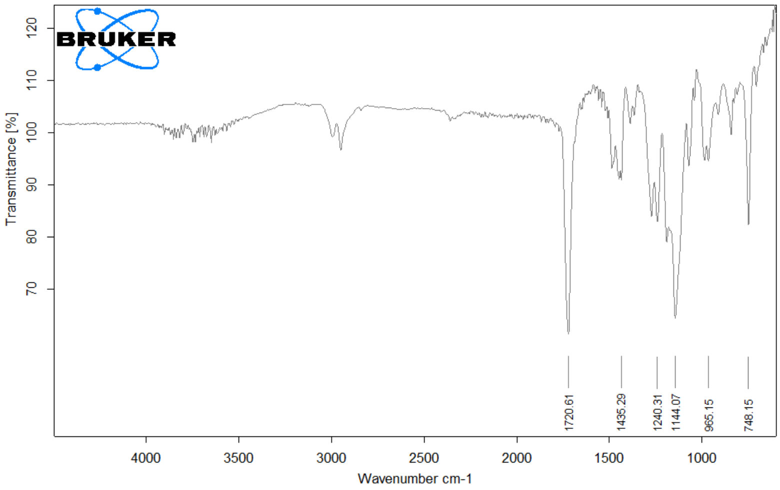

4wt%

Figure 6. FTIR spectra for nanocomposites.

3.2.2 Optical properties

The displays absorbance spectra for nanocomposites, Figure 7 show a definite relationship on the quantity of Fe_2O_3/GO and absorbance. In keeping with its optical transparency and broad band gap, pure PMMA shows minimal absorption. However, the absorbance significantly rises with the addition of Fe_2O_3/GO, especially in the visible region, as a result of many synergistic effects: Through charge-transfer transitions ($O^{2-} \rightarrow Fe^{3+}$), Fe_2O_3 nanoparticles enhance absorbance in the visible range. Graphene oxide extends light absorption towards longer wavelengths by introducing π–π^* transitions from its sp^2 hybridized carbon domains. The creation of localized electronic states is facilitated by the interfacial charge transfer between PMMA, GO, and Fe_2O_3. The composite materials' enhanced optical coupling and photo-response capabilities are demonstrated by this cumulative behavior. Increased electronic delocalization is reflected in the observed redshift (moving of the absorption edge to longer wavelengths) with increasing doping suggesting partial semiconducting nature in the modified PMMA matrix. PMMA is essentially changed from a passive optical medium into an active photo-absorbing hybrid appropriate for optoelectronic and photonic applications by Fe_2O_3 and GO nanoparticles. As the concentration of nanofiller increases, transmittance falls inversely with absorbance. High transparency is maintained by pure PMMA; however, at 4 weight percent Fe_2O_3/GO, transparency drops because Fe_2O_3 and GO phases increase optical absorption, increased scattering centers and surface roughness. Internal reflections from domains with a high refractive index. The films maintain their optical activity and semi-transparency in spite of this decrease, adding utility while maintaining PMMA's flexibility and visual clarity. Solar-control films, optical filters, and smart window coatings all depend on this regulated modulation of transmittance.

The experimental UV–visible spectra show enhanced absorbance and a redshift of the absorption edge with Fe_2O_3/GO incorporation, which is consistent with TD-DFT predictions of π–π^* and Fe–O–C charge-transfer transitions. Although experimental spectra are broadened compared to theoretical discrete peaks, both approaches confirm electronic-structure-driven optical enhancement.

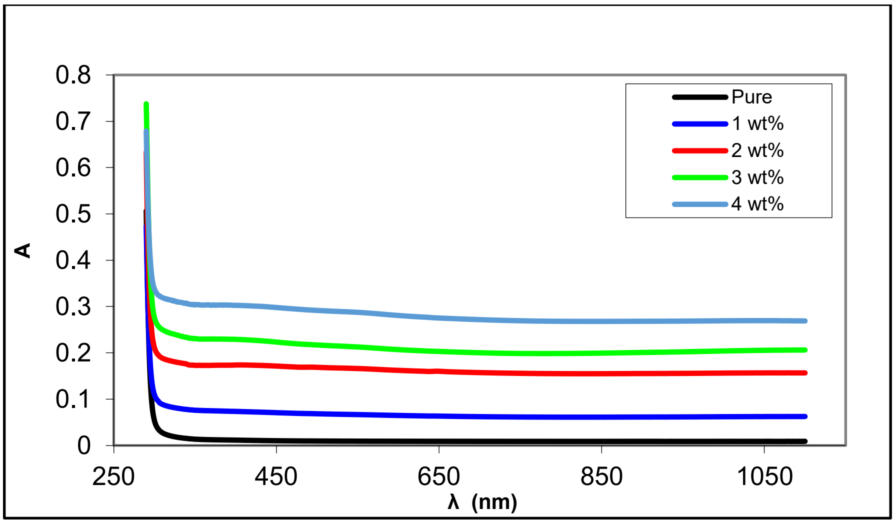

Figure 7. Shows the absorbance for nanocomposites.

Coefficient of extinction (k) in Figure 8 especially in the UV area, the extinction coefficient rises as the Fe_2O_3/GO ratio grows. Higher light attenuation from both absorption and scattering is the cause of this increase, as GO produces localized conductive domains and Fe_2O_3 offers electronic transitions. A useful feature for creating absorbing or shielding materials is adjustable optical losses, which are shown by the significant dependency of k on composition.

In Figure 9, the refractive index (n) as the amount of additives increases, the nanocomposites' refractive index steadily rises, Fe–O and C–O dipoles were added, increasing polarizability. Interfacial polarization and electronic density are increased. Localized surface plasmon-like reactions are formed at the Fe_2O_3/GO contacts. More optical density and light confinement capabilities are reflected in the rise in n, which is important for thin-film optics, waveguides, and sensors. It also indicates that the composite's electrical coupling and microstructural organization have improved.

Dielectric constants (ε_1, ε_2) in Figure 10, energy loss is represented by the imaginary component (ε_2), but energy storage is represented by the real part (ε_1). Higher Fe_2O_3/GO loading results in a rise in both components, indicating improved conductivity and polarization. Stronger dipole alignment with an applied electromagnetic field is indicated by an increase in ε_1, whilst free carrier absorption and interfacial relaxation processes are responsible for the increase in ε_2. These findings support the shift from a dielectric polymer to a hybrid that is semiconducting or weakly conducting, a change that is directly related to the enhanced charge delocalization and smaller optical band gap.

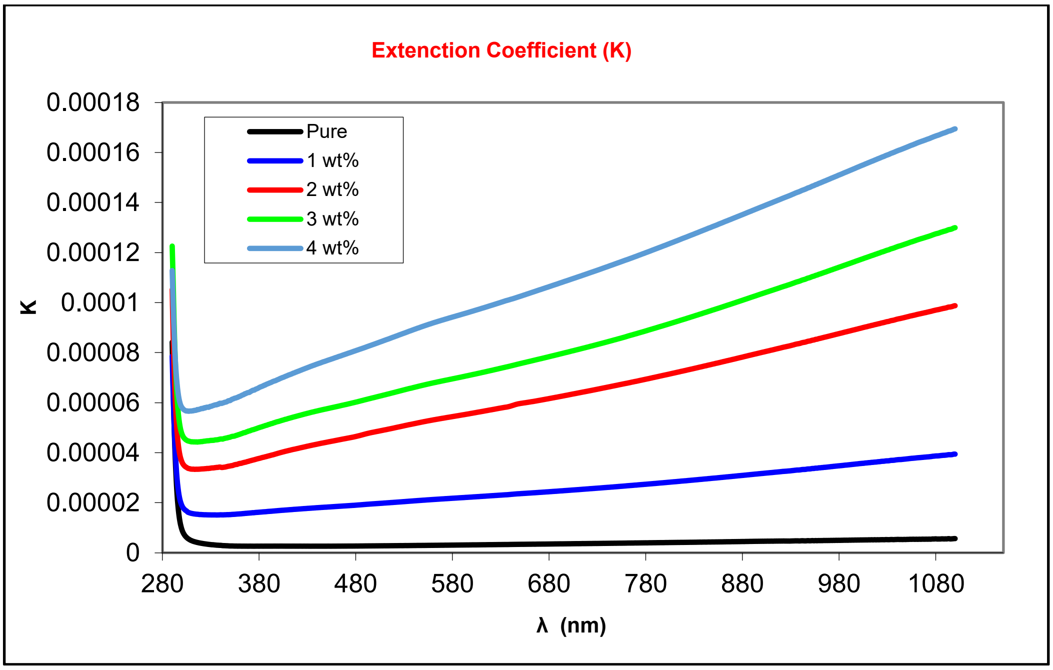

Figure 8. Shows the Extenction Coefficient for nanocomposites.

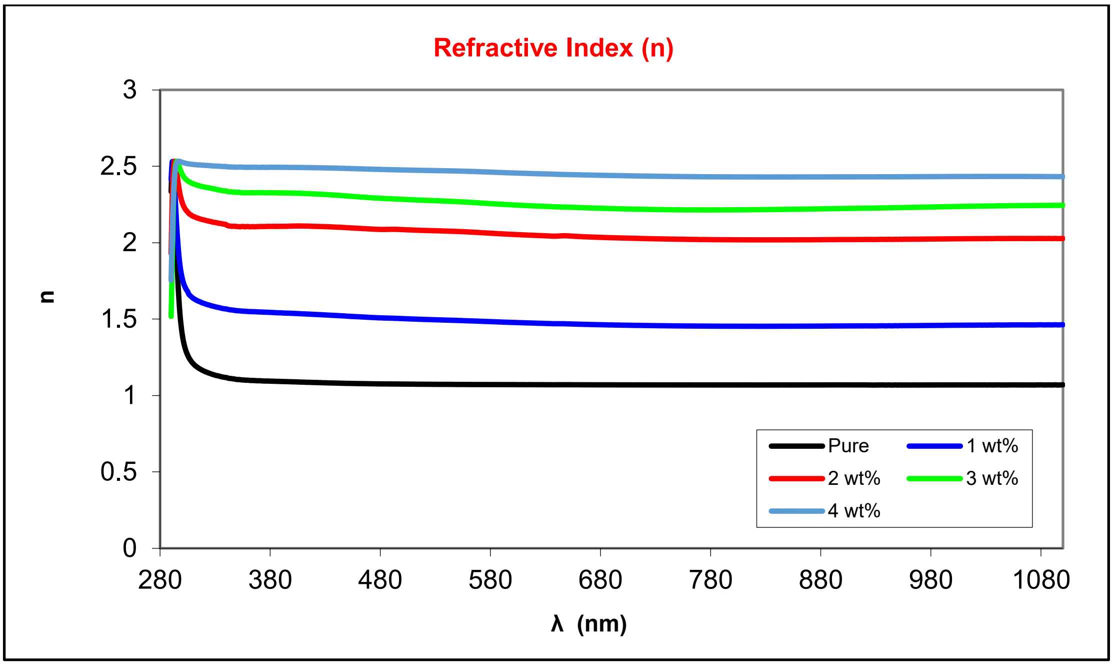

Figure 9. Shows the Refractive Index for nanocomposites.

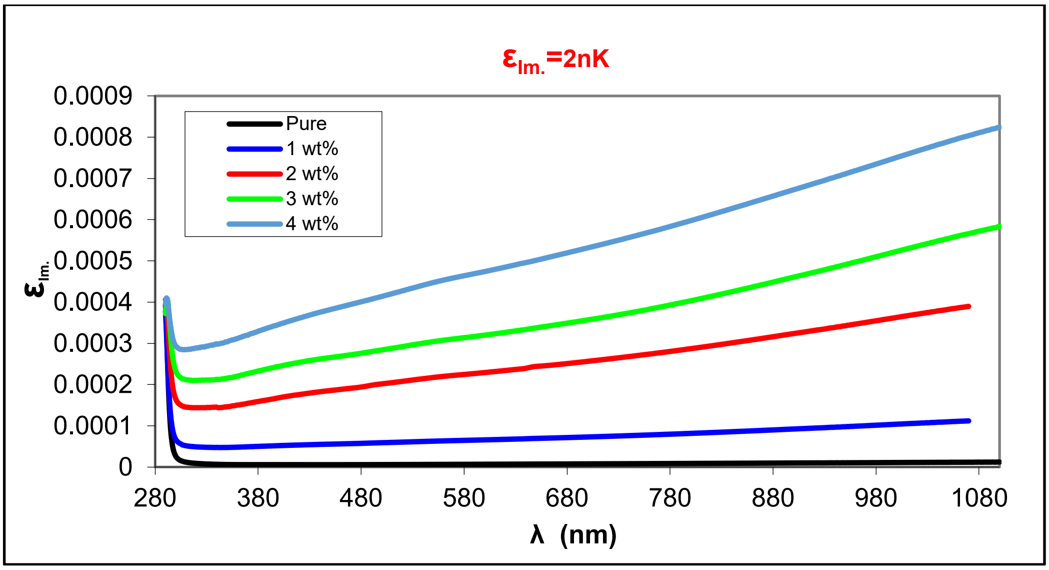

Figure 10. Shows the ε_{Im} for nanocomposites.

Figure 11 shows the optical conductivity(σ_{opt}) steadily rises as the Fe_2O_3/GO level increasing. This is a clear indication of increased charge carrier mobility and density because of a smaller band gap that makes electrical transitions simpler, enhanced channels for percolation through GO sheets and improved charge transport across the interface between nanofillers and polymer chains. The composite's photo-induced electronic activity is highlighted by the increase in σ_{opt}, which qualifies it for use in optoelectronic films, photodetectors, and photocatalysts.

Figure 12 shows the energy band gap (Eg). Eg steadily decreases from around 4.08 eV (pure PMMA) to about 3.78 eV (4 wt% Fe_2O_3/GO). The formation of defect states close to the Fermi level is reflected in this drop. Coordination bonding in Fe_2O_3 and π–π interaction in GO result in charge delocalization. A synergistic electronic interaction inside the composite is indicated by this systematic band-gap narrowing, which turns PMMA from an insulating matrix into a semiconducting hybrid with adjustable optical and electrical characteristics. While DFT calculations show a reduced HOMO-LUMO gap (1.47-1.26) eV. Although the absolute values differ, both results consistently confirm band-gap narrowing driven by electronic-structure modification and interfacial charge transfer.

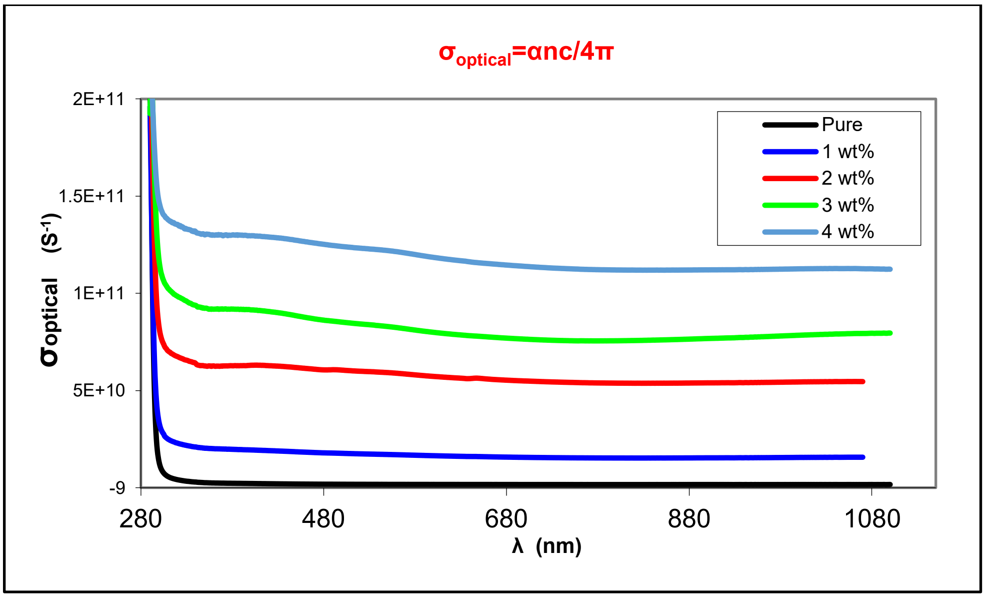

Figure 11. Shows the σ optical for nanocomposites.

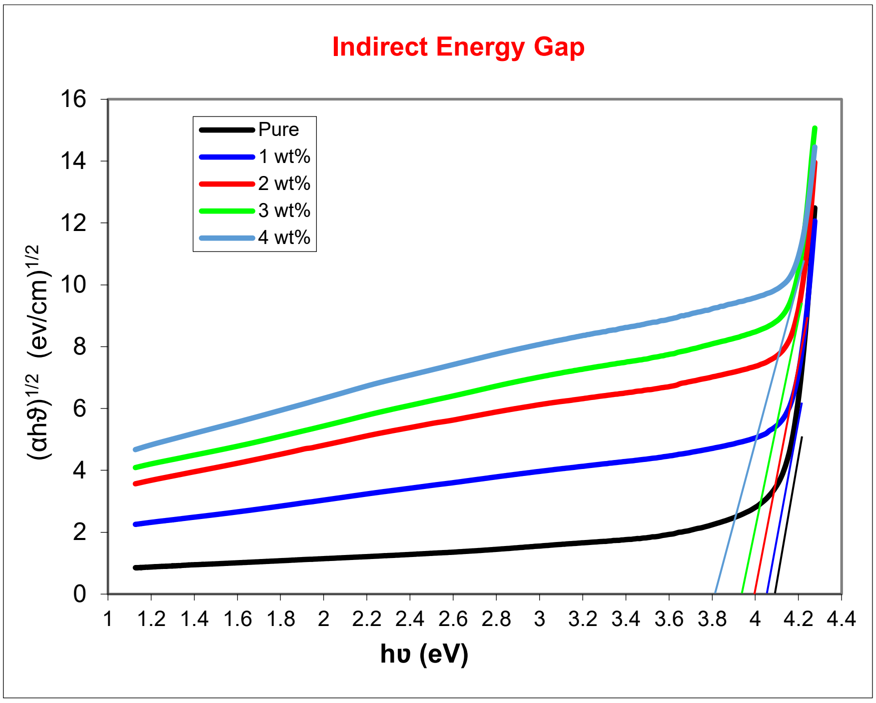

Figure 12. Energy gap values for allowed indirect transitions of nanocomposites.

3.3. Antibacterial properties

The antibacterial evaluation of the PMMA nanocomposites showed that the addition of Fe_2O_3 and GO nanoparticles significantly reduced the development of bacterial colonies as in Figure 13. Colony-forming units (CFUs) varied from 524 in the control PMMA pure to 112, 25, 19, and 3 in the modified samples, which corresponded to survival rates of 21.37%, 4.77%, 3.62%, and 0.57%, respectively. This significant decrease, which exceeded 99% inhibition in the composite with the greatest nanoparticle load, suggests a potent antibacterial activity that gets stronger as the quantity of nanoparticles increases. In line with studies from other nanocomposite systems, these results show that adding Fe2O3 and GO to PMMA gives the polymer does-dependent antibacterial activity [22, 48]. Where the sharp decline in CFU values—from524 colonies in pure PMMA to only 3 colonies with 4wt% nanofiller loading— indicates a change from a surface that is biologically passive to one that is strongly antibacterial. The success of the hybrid nanocomposite design is confirmed by this decrease, which exceeds 99% bacterial suppression at higher filler concentrations. The PMMA/Fe_2O_3/GO nanocomposites' antibacterial activity results from a variety of physicochemical processes as opposed to a single, dominating route. By producing reactive oxygen species that cause lipid peroxidation, protein denaturation, and DNA damage in bacterial cells, iron oxide nanoparticles mainly contribute through oxidative stress pathways. Bacterial inactivation results from these ROS-mediated actions, which interfere with vital cellular processes. Because increasing loadings result in a higher density of ROS-generating sites, this process becomes more effective as the concentration of nanoparticles increases.

At the same time, direct physical and interfacial antibacterial interactions depend heavily on graphene oxide. Bacterial cell membranes can be penetrated and ruptured by the sharp edges and high aspect ratio of GO nanosheets, resulting in intracellular content leakage and membrane potential loss. Furthermore, GO's oxygen-containing functional groups enable powerful hydrogen-bonding and electrostatic interactions with bacterial surfaces, further undermining the integrity of the membrane. These contact-based mechanisms work especially well against bacteria that form biofilms because they prevent initial adhesion and colony formation. The hybrid PMMA/Fe_2O_3/GO system's improved antibacterial efficacy is ascribed to the synergistic interaction between GO and Fe_2O_3. By acting as a structural scaffold, GO prevents aggregation and maximizes the effective surface area of Fe_2O_3 nanoparticles by improving their dispersion and accessibility. This better dispersion encourages consistent antibacterial action throughout the composite surface and raises the likelihood of nanoparticle–bacteria contact. Furthermore, interfacial charge transfer between GO and Fe_2O_3 may increase the efficiency of ROS formation, accelerating bacterial inactivation. A cumulative improvement of antibacterial mechanisms, such as greater surface roughness, a larger density of active sites, and better interfacial contacts with bacterial cells, is reflected in the gradual drop in CFU counts with increasing nanofiller concentration. Crucially, the retained transparency and stable hybrid network seen in optical and FTIR investigations show that this antibacterial increase takes place without sacrificing the optical and structural integrity of the PMMA matrix.

Overall, our results demonstrate a distinct link between structure, property, and bioactivity in PMMA/ Fe_2O_3/GO nanocomposites, where controlled nanofiller inclusion allows for simultaneous regulation of antibacterial activity and optical characteristics. These nanocomposites' remarkable antibacterial efficacy, material stability, and biocompatibility make them attractive options for wound-contact materials, implant coatings, and infection-resistant biomedical equipment.

Table 4. Number of cell count.

1wt%	*2wt%*	*3wt%*	*4wt%*
$212*10^{-1}$	$100*10^{-1}$	$21*10^{-1}$	$11*10^{-1}$
$192*10^{-2}$	$98*10^{-2}$	$19*10^{-2}$	$3*10^{-2}$
$183*10^{-3}$	$81*10^{-3}$		
$176*10^{-4}$	$73*10^{-4}$		
$171*10^{-5}$	$59*10^{-5}$		
$150*10^{-6}$	$25*10^{-6}$		
$124*10^{-7}$			
$112*10^{-8}$			

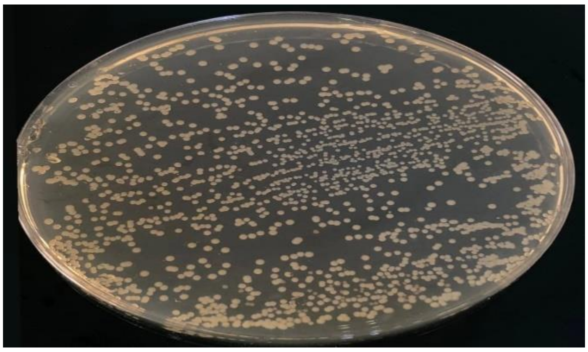

Pure

1wt%

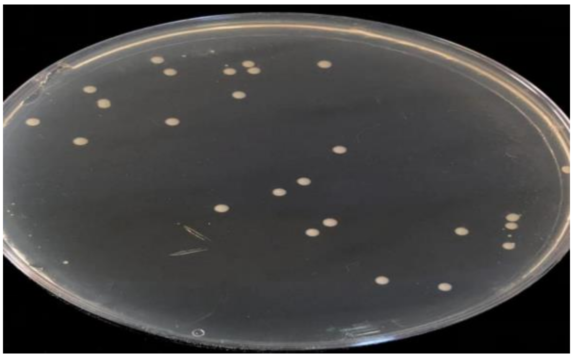

2wt%

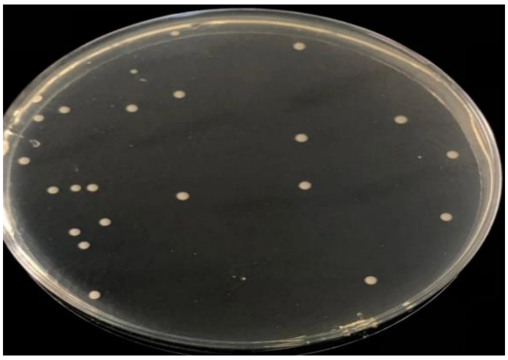

3wt%

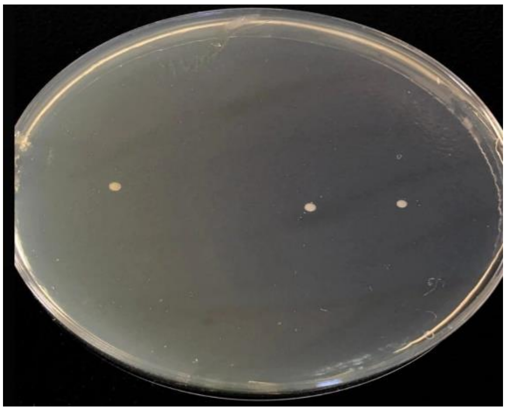

4wt%

Figure 13. Direct culture count of tested specimens according to Fe_2O_3 and GO concentrations.

4. Conclusion

The incorporation of Fe_2O_3 and GO fundamentally redefines PMMA from an inert dielectric polymer into a multifunctional, electronically active nanocomposite. Absorption-edge redshift, systematic band-gap narrowing, and simultaneous augmentation of refractive index, dielectric constant, and optical conductivity are experimental manifestations of the strong electronic-structure rearrangement caused by strong interfacial bonding and hybrid network development. Increased electronic delocalization, interfacial polarization, and effective charge-transfer channels inside the composite are all reflected in these changes.

DFT and TD-DFT analyses provide direct mechanistic validation, revealing reduced HOMO–LUMO gaps, redistributed frontier orbitals, and charge-transfer excitations associated with Fe–O–C and π–π* interactions. Surface reactivity and optical response are controlled by electrostatically active interfaces, which are further confirmed by the stabilized and increased molecule electrostatic potential. Film-level collective effects are the source of small differences between theoretical and experimental spectra, which do not change the underlying electronic trends. Beyond optoelectronic tunability, the hybrid nanocomposites demonstrate exceptional antibacterial activity, surpassing 99% inhibition via a synergistic mechanism that combines graphene oxide-mediated membrane rupture and iron oxide-induced oxidative stress.

PMMA/FeO_3/GO is positioned as a strong platform for cutting-edge optoelectronic and infection-resistant biomedical applications after our results, which establish electronic-structure engineering as a cohesive approach for concurrently manipulating optical, electroactive, and antibacterial functions.

References

1. Díez-Pascual AM, Luceño-Sánchez JA (2021) Antibacterial activity of polymer nanocomposites incorporating graphene and its derivatives: A state of art. Polymers (Basel) 13:2105https://www.mdpi.com/2073-4360/13/13/2105
2. Pavithra D, Doble M (2008) Biofilm formation, bacterial adhesion and host response on polymeric implants—issues and prevention. Biomedical Materials 3:034003 https://iopscience.iop.org/article/10.1088/1748-6041/3/3/034003/meta
3. Veerachamy S, Yarlagadda T, Manivasagam G, Yarlagadda PKD V (2014) Bacterial adherence and biofilm formation on medical implants: a review. Proc Inst Mech Eng H 228:1083–1099 https://journals.sagepub.com/doi/abs/10.1177/0954411914556137
4. SJ A, Natarajan A (2022) Review on the advancements and relevance of emerging joining techniques for aluminium to polymers/carbon fibre-reinforced polymer lightweight hybrid structures. Proceedings of the Institution of Mechanical Engineers, Part L: Journal of Materials: Design and Applications 236:2394–2435 https://journals.sagepub.com/doi/abs/10.1177/14644207221090331
5. Xiong R, Luan J, Kang S, Ye C, Singamaneni S, Tsukruk V V (2020) Biopolymeric photonic structures: design, fabrication, and emerging applications. Chem Soc Rev 49:983–1031 https://pubs.rsc.org/en/content/articlehtml/2020/cs/c8cs01007b
6. Mammeri F, Le Bourhis E, Rozes L, Sanchez C (2005) Mechanical properties of hybrid organic–inorganic materials. J Mater Chem 15:3787–3811 https://pubs.rsc.org/en/content/articlehtml/2005/jm/b507309j
7. Díez-Pascual AM, Luceño-Sánchez JA (2021) Antibacterial activity of polymer nanocomposites incorporating graphene and its derivatives: A state of art. Polymers (Basel) 13:2105 https://www.mdpi.com/2073-4360/13/13/2105
8. Pavithra D, Doble M (2008) Biofilm formation, bacterial adhesion and host response on polymeric implants—issues and prevention. Biomedical Materials 3:034003 https://iopscience.iop.org/article/10.1088/1748-6041/3/3/034003/meta
9. Veerachamy S, Yarlagadda T, Manivasagam G, Yarlagadda PKD V (2014) Bacterial adherence and biofilm formation on medical implants: a review. Proc Inst Mech Eng H 228:1083–1099 https://journals.sagepub.com/doi/abs/10.1177/0954411914556137
10. SJ A, Natarajan A (2022) Review on the advancements and relevance of emerging joining techniques for aluminium to polymers/carbon fibre-reinforced polymer lightweight hybrid structures. Proceedings of the Institution of Mechanical Engineers, Part L: Journal of Materials: Design and Applications 236:2394–2435 https://journals.sagepub.com/doi/abs/10.1177/14644207221090331
11. Xiong R, Luan J, Kang S, Ye C, Singamaneni S, Tsukruk V V (2020) Biopolymeric photonic structures: design, fabrication, and emerging applications. Chem Soc Rev 49:983–1031 https://pubs.rsc.org/en/content/articlehtml/2020/cs/c8cs01007b
12. Mammeri F, Le Bourhis E, Rozes L, Sanchez C (2005) Mechanical properties of hybrid organic–inorganic materials. J Mater Chem 15:3787–3811 https://pubs.rsc.org/en/content/articlehtml/2005/jm/b507309j
13. Ali U, Karim KJBA, Buang NA (2015) A review of the properties and applications of poly (methyl methacrylate)(PMMA). Polymer Reviews 55:678–705 https://www.tandfonline.com/doi/abs/10.1080/15583724.2015.1031377
14. Hazim A, Abduljalil HM, Hashim A (2021) Design of PMMA doped with inorganic materials as promising structures for optoelectronics applications. Transactions on Electrical and Electronic Materials 22:851–868 https://link.springer.com/article/10.1007/s42341-021-00308-1
15. Alias AN, Zabidi ZM, Ali AMM, Harun MK, Yahya MZA (2013) Optical characterization and properties of polymeric materials for optoelectronic and photonic applications. Int J Appl Sci Technol 3: https://www.academia.edu/download/34111519/ijastnet.com_journals_Vol_3_No_5_May_2013_3.pdf
16. Ali U, Karim KJBA, Buang NA (2015) A review of the properties and applications of poly (methyl methacrylate)(PMMA). Polymer Reviews 55:678–705 https://www.tandfonline.com/doi/abs/10.1080/15583724.2015.1031377
17. Zafar MS (2020) Prosthodontic applications of polymethyl methacrylate (PMMA): An update. Polymers (Basel) 12:2299 https://www.mdpi.com/2073-4360/12/10/2299

18. Burcea A, Bănățeanu A-M, Poalelungi C-V, Forna N, Cumpătă CN (2024) Enhanced properties and multifaceted applications of polymethyl methacrylate (PMMA) in modern medicine and dentistry. Rom J Oral Rehabil 16:108–123 http://rjor.ro/wp-content/uploads/2024/12/ENHANCED-PROPERTIES-AND-MULTIFACETED-APPLICATIONS-OF-POLYMETHYL-METHACRYLATE-PMMA-IN-MODERN-MEDICINE-AND-DENTISTRY-1.pdf
19. Edo GI, Ndudi W, Ali ABM, Yousif E, Zainulabdeen K, Onyibe PN, Akpoghelie PO, Ekokotu HA, Isoje EF, Igbuku UA (2024) An updated review on the modifications, recycling, polymerization, and applications of polymethyl methacrylate (PMMA). J Mater Sci 59:20496–20539 https://link.springer.com/article/10.1007/s10853-024-10402-3
20. Kreve S, Dos Reis AC (2025) Antibiofilm capacity of PMMA surfaces: A review of current knowledge. Microb Pathog 107426 https://www.sciencedirect.com/science/article/pii/S0882401025001512
21. Ahmad H, Fan M, Hui D (2018) Graphene oxide incorporated functional materials: A review. Compos B Eng 145:270–280 https://www.sciencedirect.com/science/article/pii/S1359836817342245
22. Yu W, Sisi L, Haiyan Y, Jie L (2020) Progress in the functional modification of graphene/graphene oxide: A review. RSC Adv 10:15328–15345 https://pubs.rsc.org/en/content/articlehtml/2020/ra/d0ra01068e
23. Dalton LR, Sullivan PA, Bale DH (2010) Electric field poled organic electro-optic materials: state of the art and future prospects. Chem Rev 110:25–55 https://pubs.acs.org/doi/full/10.1021/cr9000429
24. Fan S, Zhang Y, Huang X, Geng L, Shao H, Hu X, Zhang Y (2019) Silk materials for medical, electronic and optical applications. Sci China Technol Sci 62:903–918 https://link.springer.com/article/10.1007/s11431-018-9403-8
25. Jain PK, Huang X, El-Sayed IH, El-Sayed MA (2008) Noble metals on the nanoscale: optical and photothermal properties and some applications in imaging, sensing, biology, and medicine. Acc Chem Res 41:1578–1586 https://pubs.acs.org/doi/abs/10.1021/ar7002804
26. Elahi N, Rizwan M (2021) Progress and prospects of magnetic iron oxide nanoparticles in biomedical applications: A review. Artif Organs 45:1272–1299 https://onlinelibrary.wiley.com/doi/abs/10.1111/aor.14027
27. Kumar S, Kumar M, Singh A (2021) Synthesis and characterization of iron oxide nanoparticles (Fe2O3, Fe3O4): a brief review. Contemp Phys 62:144–164 https://www.tandfonline.com/doi/abs/10.1080/00107514.2022.2080910
28. Pourmadadi M, Rahmani E, Shamsabadipour A, Mahtabian S, Ahmadi M, Rahdar A, Díez-Pascual AM (2022) Role of iron oxide (Fe2O3) nanocomposites in advanced biomedical applications: a state-of-the-art review. Nanomaterials 12:3873 https://www.mdpi.com/2079-4991/12/21/3873
29. Al-Bataineh QM, Ahmad AA, Alsaad AM, Telfah AD (2021) Optical characterizations of PMMA/metal oxide nanoparticles thin films: bandgap engineering using a novel derived model. Heliyon 7: https://www.cell.com/heliyon/fulltext/S2405-8440(21)00057-8
30. Mosleh AT, Yousef TA, Khairy M, Ferjani H, Almuhana ARY, Zahran HY, Rahman A El, Essam OA, Abdelnasser MI, Abdelbaset SA (2025) Multifunctional prospects of PMMA/Fe2O3@ NiO nanocomposite membranes: advanced optical, dielectric, and photocatalytic properties for electronic optoelectronic devices, and environmental applications. J Solgel Sci Technol 1–20 https://link.springer.com/article/10.1007/s10971-025-06875-6
31. Gomaa F, Moustapha ME, Mohammed MI (2025) Optical tunable, electrical, thermal stable, and photocatalytic properties of PMMA/Fe2O3 nanocomposite films. Journal of Umm Al-Qura University for Applied Sciences 1–19 https://link.springer.com/article/10.1007/s43994-025-00250-5
32. Ul-Haq Y, Murtaza I, Mazhar S, Ullah R, Iqbal M, Qarni AA, Amin S (2020) Dielectric, thermal and mechanical properties of hybrid PMMA/RGO/Fe2O3 nanocomposites fabricated by in-situ polymerization. Ceram Int 46:5828–5840 https://www.sciencedirect.com/science/article/pii/S0272884219332110
33. Costa B, Martínez-de-Tejada G, Gomes PAC, L. Martins MC, Costa F (2021) Antimicrobial peptides in the battle against orthopedic implant-related infections: A review. Pharmaceutics 13:1918 https://www.mdpi.com/1999-4923/13/11/1918
34. Kumar P, Huo P, Zhang R, Liu B (2019) Antibacterial properties of graphene-based nanomaterials. Nanomaterials 9:737 https://www.mdpi.com/2079-4991/9/5/737
35. Idisi DO, Aigbe UO, Ahia CC, Meyer EL (2023) Graphene oxide: Fe2O3 nanocomposite: synthesis, properties, and applications. Carbon Letters 33:605–640 https://link.springer.com/article/10.1007/s42823-023-00469-4
36. Elawady R, Aboulela AG, Gaballah A, Ghazal AA, Amer AN (2024) Antimicrobial Sub-MIC induces Staphylococcus aureus biofilm formation without affecting the bacterial count. BMC Infect Dis 24:1065 https://link.springer.com/article/10.1186/s12879-024-09790-3
37. Bankier C, Cheong Y, Mahalingam S, Edirisinghe M, Ren G, Cloutman-Green E, Ciric L (2018) A comparison of methods to assess the antimicrobial activity of nanoparticle combinations on bacterial cells. PLoS One 13:e0192093 https://journals.plos.org/plosone/article?id=10.1371/journal.pone.0192093
38. Wilson C, Lukowicz R, Merchant S, Valquier-Flynn H, Caballero J, Sandoval J, Okuom M, Huber C, Brooks TD, Wilson E (2017) Quantitative and qualitative assessment methods for biofilm growth: a mini-review. Res Rev J Eng Technol 6:http-www https://pmc.ncbi.nlm.nih.gov/articles/PMC6133255/

39. Zhang X, Hou X, Ma L, Shi Y, Zhang D, Qu K (2023) Analytical methods for assessing antimicrobial activity of nanomaterials in complex media: advances, challenges, and perspectives. J Nanobiotechnology 21:97 https://link.springer.com/article/10.1186/s12951-023-01851-0
40. Hassan AK, Hamidinezhad H, Al-Bermany E (2024) Antibacterial activity and optical behavior for restoration of micro and nano dental fillers using functional graphene nanosheets with polymethyl methacrylate. Nano Biomed Eng 16:652–664 https://www.academia.edu/download/121467162/1794956328848433153.pdf
41. Butler J, Handy RD, Upton M, Besinis A (2023) Review of antimicrobial nanocoatings in medicine and dentistry: mechanisms of action, biocompatibility performance, safety, and benefits compared to antibiotics. ACS Nano 17:7064–7092 https://pubs.acs.org/doi/abs/10.1021/acsnano.2c12488
42. Gadre SR, Suresh CH, Mohan N (2021) Electrostatic potential topology for probing molecular structure, bonding and reactivity. Molecules 26:3289 https://www.mdpi.com/1420-3049/26/11/3289
43. Suresh CH, Remya GS, Anjalikrishna PK (2022) Molecular electrostatic potential analysis: A powerful tool to interpret and predict chemical reactivity. Wiley Interdiscip Rev Comput Mol Sci 12:e1601 https://wires.onlinelibrary.wiley.com/doi/abs/10.1002/wcms.1601
44. Guin M, Halder S, Chatterjee S, Konar S (2022) Synthesis, X-ray crystal structure of Cu (II) 1D coordination Polymer: In View of Hirshfeld surface, FMO, Molecular electrostatic potential (MEP) and Natural Bond orbital (NBO) analyses. J Mol Struct 1270:133949 https://www.sciencedirect.com/science/article/pii/S0022286022016027
45. Abdulsattar MA, Abduljalil HM, Abed HH (2019) Formation energies of CdSe wurtzoid and diamondoid clusters formed from Cd and Se atomic clusters. Calphad 64:37–42 https://www.sciencedirect.com/science/article/pii/S036459161830169X
46. Abduljalil HM, Hadi NA-HS, Abed HH (2025) Investigation of the impact of DMSO and H2O solvents on the electronic and photovoltaic properties of graphene-oxide nanostructures: A DFT study. Struct Chem 1–11 https://link.springer.com/article/10.1007/s11224-025-02700-6
47. Kim J-S, Shin D-H (2013) Inhibitory effect on Streptococcus mutans and mechanical properties of the chitosan containing composite resin. Restor Dent Endod 38:36 https://synapse.koreamed.org/pdf/10.5395/rde.2013.38.1.36
48. Alzayyat ST, Almutiri GA, Aljandan JK, Algarzai RM, Khan SQ, Akhtar S, Matin A, Gad MM (2021) Antifungal efficacy and physical properties of poly (methylmethacrylate) denture base material reinforced with SiO2 nanoparticles. Journal of Prosthodontics 30:500–508 https://onlinelibrary.wiley.com/doi/abs/10.1111/jopr.13271
49. ZąBkowska ‐ Wacławek M, Talik P, Wacławek W (1990) On the Compensation Behaviour of Copper Phthalocyanine Films in NOx Ambient. physica status solidi (a) 121:489–494 https://onlinelibrary.wiley.com/doi/abs/10.1002/pssa.2211210217
50. Kazmarski L, Clark A (1980) Polycrystalline and Amorphouse Thin Films and Device. Lawrence Academic Press, New York 267:142
51. Grenier R (1961) Semiconductors device and electronic energy series
52. Moss TS (1959) Optical Properties of Semiconductors, London Table (1): illustrate the values of Eg as a function of Ta. Ta (K) Eg"(eV) RT () S 4:
53. Aguilar-Perez D, Vargas-Coronado R, Cervantes-Uc JM, Rodriguez-Fuentes N, Aparicio C, Covarrubias C, Alvarez-Perez M, Garcia-Perez V, Martinez-Hernandez M, Cauich-Rodriguez JV (2020) Antibacterial activity of a glass ionomer cement doped with copper nanoparticles. Dent Mater J 39:389–396 https://www.jstage.jst.go.jp/article/dmj/39/3/39_2019-046/_article/-char/ja/
54. Hosseinzadeh H (2025) Antibacterial/Magnetic Iron Oxide Nanoparticles: A Comprehensive Review of Synthesis Methods, Doping Effects, Antibacterial Properties, and Applications in Medical and Food Industries. Journal of Applied Material Science 1:e210146 https://jams.hsu.ac.ir/article_226617.html